CC BY

Biosynthesized Mn_2O_3 nanoparticles from Syzygium alternifolium leaf extract: Structural characterization, Crystal violet dye degradation, and Antibacterial activity

Surada Dhanaraj[1,2], Kommu Jayarao[3*], Gopi Mamidi[2], Ramarao Vangara[4], Voosala Christopher[1]

[1]Dept.of Chemistry, Andhra University, Visakhapatnam-530003, India
[2]Dept. of Chemistry, Dr.V.S.Krishna Govt. Degree College (A), Visakhapatnam-530013, India
[2]Dept. of Chemistry, Welfare Institute of Science, Technology & Management, Pendurthi-531173, India
[3]Dept. of Chemistry, Maharajah's College(A), Vizianagaram-535002, India
*Correspondence email: jayaraokommu1@gmail.com;

Abstract
The green synthesis, characterisation, photocatalytic, and antibacterial assessment of Mn_2O_3 nanoparticles made with Syzygium alternifolium leaf extract are presented in this study. The synthesized α- Mn_2O_3 NPs were characterized by UV-Vis, XRD, FTIR, SEM-EDX, and TGA analyses, confirming phase-pure cubic crystallinity, nanoscale morphology, thermal stability, and elemental purity. SEM images revealed agglomerated spherical nanostructures, while EDX confirmed manganese and oxygen as the predominant elements. The biosynthesized α-Mn_2O_3 NPs exhibited excellent visible-light-driven photocatalytic activity toward crystal violet dye degradation, achieving nearly 99% efficiency under optimized conditions, particularly at alkaline pH. Photocatalytic performance was significantly influenced by pH, catalyst dosage, dye concentration, and irradiation time, with reactive oxygen species (•OH and O_2•$^-$ radicals) playing a key role in dye mineralization. The nanoparticles also demonstrated notable stability and reusability over five cycles. Additionally, the Mn_2O_3 NPs showed significant concentration-dependent antibacterial activity against S.aureus and E.coli, attributed to oxidative stress and membrane disruption.

Keywords: Syzygium alternifolium; Mn_2O_3 nanoparticles; Crystal violet degradation; Antibacterial activity

1. Introduction

One of the most important environmental issues of the twenty-first century is water pollution caused by the careless release of synthetic dyes into aquatic environments [1]. According to estimates, 8-20% of all dyestuffs used worldwide are discharged into the water environment as a result of their synthesis and textile industry activities, endangering ecological integrity, aquatic biodiversity, and human health [2]. Wastewater containing dye poses serious environmental risks and has detrimental effects on human health as well as the health of other organisms that make up the ecosystem [3]. Crystal Violet (CV), a triphenylmethane-class cationic dye, is one of the most widely used industrial dyes in textile processing, paper production, biological staining, and medicinal applications [4]. Despite its widespread use, CV is carcinogenic to humans and remains in industrial effluents for a long time, making its persistence in water bodies a top ecotoxicological issue. The structural complexity, chromophoric stability, and non-biodegradable nature of triphenylmethane compounds like CV make conventional physicochemical methods for treating textile effluents expensive and energy-intensive, making the development of sophisticated, sustainable remediation technologies necessary [5-6].

Metal oxide nanoparticle (NPs) based photocatalytic degradation has gained significant traction as an environmentally friendly and effective method for breaking down stubborn organic coloring contaminants [7]. By capturing light energy and producing reactive oxygen species (ROS) such hydroxyl radicals (•OH) and superoxide anions (O_2•$^-$) that break the chromophoric bonds of dye molecules, the photocatalyst helps oxidation and reduction processes [8]. For the photocatalytic degradation of Crystal Violet, several metal oxide systems, such as TiO_2, ZnO, Fe_2O_3, CuO, MgO, and NiO, have been assessed. For example, under ideal pH, catalyst dosage, and dye concentration circumstances, MgO nanoparticles and MgO-bentonite nanocomposites have been demonstrated to reach maximum CV degradation efficiencies of 99.19% and 83.38%, respectively. The photocatalytic breakdown of Crystal Violet dye under sunlight has also been studied for green-synthesised iron oxide nanoparticles, underscoring the increasing interest in environmentally acceptable nanomaterial platforms for dye remediation [9-11].

Serious environmental and public health issues have been raised by the sharp rise in dye pollution and multidrug-resistant bacteria. The capacity of metal oxide nanoparticles (MnO NPs) to produce ROS, which aid in the photocatalytic degradation of organic pollutants and antibacterial activity against pathogenic microorganisms like E.coli and S.aureus, has garnered a lot of attention. Because of their superior redox characteristics, low toxicity, and significant photocatalytic and antibacterial potential, manganese oxide nanoparticles stand out among them [12-14].

An economical and environmentally beneficial substitute for traditional nanoparticle production techniques is green synthesis, which uses plant extracts. Flavonoids, phenols, and terpenoids are examples of phytochemicals

derived from plants that function as natural reducing and stabilizing agents during the production of nanoparticles [15]. However, there is still much to learn about the synthesis of MnO NPs utilizing S.alternifolium leaf extract and their combined use in crystal violet dye degradation and antibacterial research against S. aureus and E.coli. In order to emphasize the potential of MnO NPs as sustainable multifunctional nanomaterials for environmental and medicinal applications, the current study focuses on the green synthesis and characterization of MnO NPs and assesses their photocatalytic and antibacterial performance.

2. Experimental part

2.1. Collection of Plant Material and Chemicals

Fresh Syzygium alternifolium leaves were collected from the vicinity of the port area in Visakhapatnam, Andhra Pradesh, India (17°44'25"N, 83°19'15"E). Ferric chloride ($FeCl_3$) with 98% of AR grade was procured from Merck, India, and used without further purification. Distilled water was employed in all experiments.

2.2. Preparation of Syzygium alternifolium Leaf Extract

Fresh Syzygium alternifolium leaves were carefully washed with tap water followed by thorough rinsing with distilled water to remove any surface contaminants. The cleaned leaves were dried under shade until completely dehydrated. The dried leaves were then ground into a fine powder using a household grinder. A quantity of 2 g of the powdered material was added to 100 mL of distilled water in a 250 mL glass beaker. The mixture was heated at 70 °C for 2 hours using a hot plate, resulting in the formation of a brown colored solution. This extract was filtered using Whatman No. 1 filter paper to remove any solid residues. The filtrate was then stored at 4 °C in a refrigerator for further use.

2.3. Synthesis of Syzygium alternifolium-capped Fe_2O_3 NPs

To synthesize Syzygium alternifolium leaves extract Fe_2O_3 NPs, 200 mL of 0.05 N $FeCl_3$ solution was taken in a 500 mL beaker and stirred for 5 minutes to ensure homogeneity. Subsequently, 50 mL of the prepared S.alternifolium leaf extract was added to the solution. The beaker was covered with aluminum foil to minimize evaporation during the reaction. The mixture was then stirred at 70 °C for 3 hours at a constant speed of 500 rpm, leading to the formation of a brown-colored suspension. The suspension was left undisturbed for 6 hours in the dark to complete the reaction. The resulting brown precipitate was filtered, and the solid was dried in a hot air oven at 60 °C for 6 hours. Finally, the dried material was ground into a fine powder using a mortar and pestle, rendering it ready for subsequent characterization.

2.4. Characterization

The structural, morphological, and magnetic characteristics of the Syzygium-synthesised-Fe_2O_3 NPs were thoroughly characterized using a variety of sophisticated analytical techniques. A D8 Bruker Kappa Apex II diffractometer operating at 40 kV and 35 mA with Cu-Kα radiation (λ = 1.54 Aº) and a 2θ range of 10º to 90º with a scan speed of 0.2 s per step was used to establish the crystalline nature and phase purity of the Syzygium-mediated Fe_2O_3 NPs. A Shimadzu IR Prestige2 spectrometer was used to record the Fourier Transform Infrared (FTIR) spectra in the 4000-400 cm^{-1} spectral region using KBr pellets in transmission mode. This allowed for the identification of functional groups that were responsible for the bioreduction and stabilization of the nanoparticles. To probe the optical properties of the synthesized NPs, UV-Visible spectroscopy was conducted using a LabIndia UV-3092 spectrophotometer and the absorbance spectrum was recorded over the 200-800 nm wavelength range at ambient temperature. Morphological features and surface topology were investigated through scanning electron microscopy (SEM) using a JEOL 6390LA instrument coupled with energy-dispersive X-ray (EDX) spectroscopy for elemental analysis and confirmation of elemental composition.

2.5. Photocatalytic experiment

The photocatalytic performance of the bio-synthesized α-Fe_2O_3 NPs was systematically evaluated for the degradation of fast green (FG) dye under visible light irradiation. In a typical experiment, 50 mL of FG dye solution with an initial concentration of 10 ppm was mixed with 50 mg of α-Fe_2O_3 NPs. To ensure adsorption-desorption equilibrium, the suspension was magnetically stirred in the dark for 30 minutes. After this stabilization period, the reaction mixture was irradiated under a metal halide lamp as visible light source, simulating indoor sunlight conditions. The experiments were conducted at ambient room temperature. During the photocatalytic process, aliquots were periodically withdrawn at regular intervals to monitor the progress of dye degradation. The collected samples were immediately centrifuged at 4000 rpm to separate the catalyst from the solution. The residual concentration of FG dye was quantified by measuring the absorbance at 624 nm using a UV-Visible spectrophotometer. The photocatalytic degradation efficiency was calculated using the following equation (1).

$$\text{Degradation } \% = \frac{A_0 - A_t}{A_o} \times 100 \qquad \text{Eq. (1)}$$

Where 'A_0' is the initial absorbance of the dye solution and 'A_t' is the absorbance at a given time't'.

2.6. Antibacterial activity

Using the agar well diffusion method, the antibacterial activity of biosynthesized hematite NPs was assessed against Gram-positive Staphylococcus aureus (ATCC 25923) and Gram-negative Escherichia coli (ATCC 25922). Mueller-Hinton agar plates were covered with standardized bacterial cultures (0.5 McFarland standard), and Fe_2O_3 NPs suspensions at 10, 50, and 100 µg/mL were added to the wells. The positive control was amoxicillin (5 µg), while the negative control was DMSO. The zones of inhibition were measured in millimeters after the plates were incubated at 37 ºC for 24 hours following pre-diffusion at 4 ºC for 30 minutes. Every experiment was carried out in triplicate.

3. Results and Discussion

3.1. Characterization analyses results

a. XRD analysis

The XRD (x-ray diffraction) of S.alternifolium leaf extract-mediated manganese oxide nanoparticles were presented in Fig.1. The XRD patterns were observed at 2θ values of 27.48°, 33.88°, 37.34°, 45.74°, 52.38°, 56.14°, 59.74°, and 61.16°, which consigned to the respective planes of (222), (400), (332), (431), (440), (611), (622), and (444), matched with JCPDS (41-1442), confirmed the formation of cubic manganese(III) oxide (α-Mn_2O_3) [16]. The great crystallinity and phase purity were signified by the strong diffraction peaks for biosynthesized NPs. The average crystalline size (S) of prepared α-Mn_2O_3 NPs was determined using Debey-scherrer's equation 1, and found to be 26.3 nm. The biosynthesized NPs may be used in treatment of wastewater due to lesser in size.

$$S = \frac{k \lambda}{\beta \cos\theta} \qquad \text{Eq. 1}$$

Where, k is scherrer's constant (0.9), 'ʎ' represents wavelength (1.54 nm), 'β' is the FWHM (full width at half-maxima, and 'θ' is the diffraction angle.

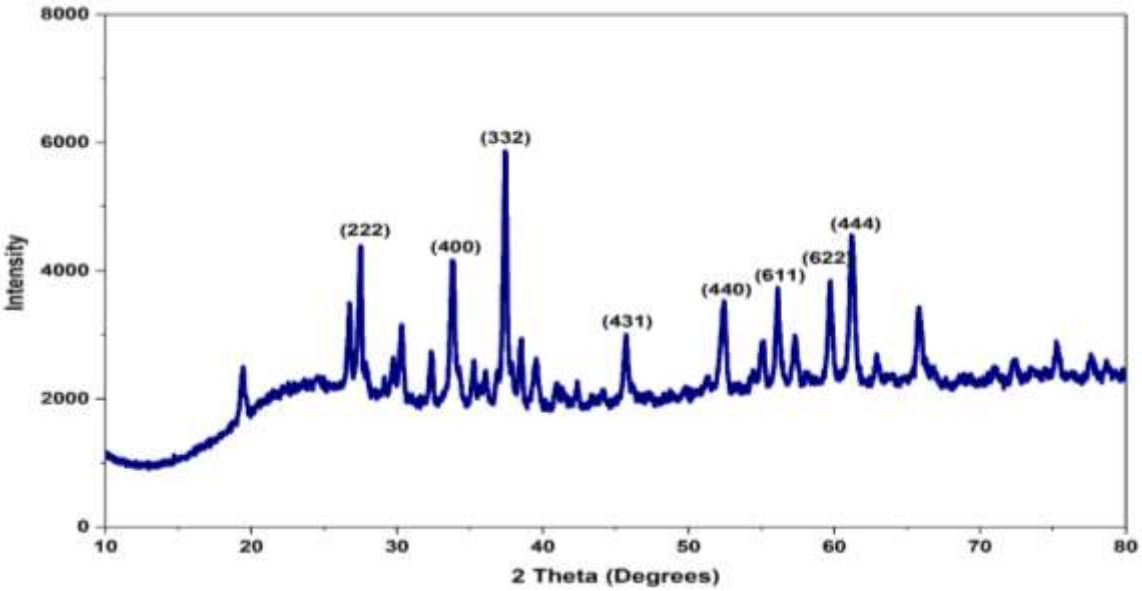

Fig.1: XRD patterns of S. alternifolium leaf extract-mediated α-Mn_2O_3 NPs

b. FTIR study

The existence of several functional groups linked to phytochemicals from Syzygium alternifolium leaf extract and their role in nanoparticle synthesis and stability were confirmed by the FTIR spectrum of the biosynthesized α-Mn_2O_3 NPs (Fig.2). The O-H stretching vibrations of hydroxyl groups found in phenols and alcohols are represented by a large absorption band seen at 3400-3500 cm^{-1}, suggesting the involvement of polyphenolic chemicals in the reduction and capping process. The C-H stretching vibrations of aliphatic hydrocarbons are responsible for the peaks about 2920-2850 cm^{-1}. While the peaks seen in the range of 1380-1450 cm^{-1} correspond to C-N stretching and bending vibrations of biomolecules, the absorption band at 1642 cm^{-1} may be attributed to C=O stretching or bending vibrations of adsorbed water molecules and amide functional groups. Crucially, the Mn-O stretching vibration is confirmed by the distinctive absorption band seen in the lower wavenumber region below 700 cm^{-1}, confirming the successful production of Mn_2O_3 NPs [16].

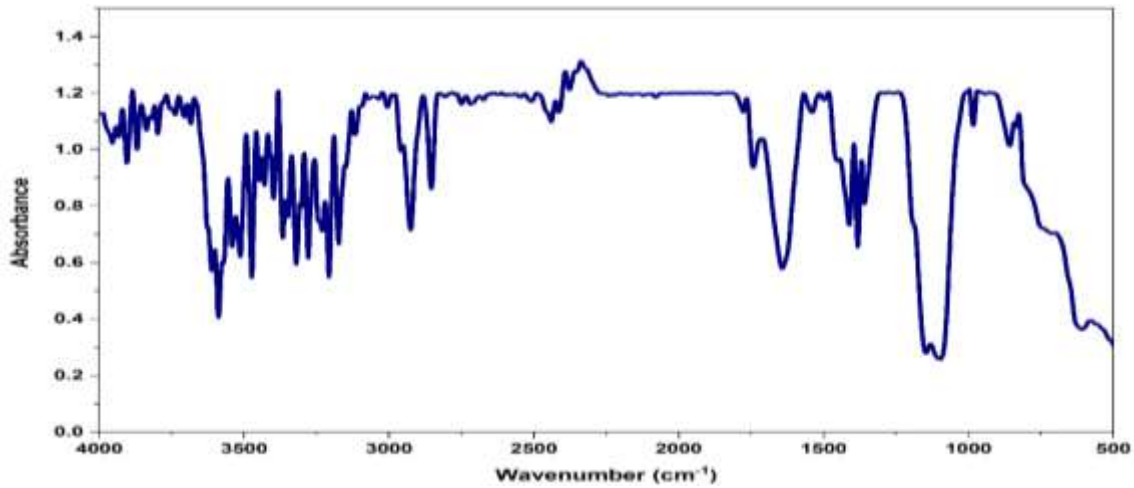

Fig.2: FTIR spectrum of Syzygium-mediated α-Mn_2O_3 NPs

c. SEM-EDX analysis

SEM and EDX investigations were used to examine the surface morphology and elemental composition of the biosynthesized manganese oxide nanoparticles, as illustrated in Fig.3 (a-c). The production of tightly packed and agglomerated nanoparticles with nearly spherical to irregular morphologies was visible in the SEM micrographs at various magnifications. The high surface energy and strong interparticle interactions frequently seen in metal oxide nanomaterials produced using environmentally friendly processes may be the reason why the particles seemed to form clustered assemblies. The majority of the nanoparticles were in the nanometer range, and their rough surface texture suggested that they had successfully nucleated and grown during the phytosynthesis process [17]. The presence of phytochemical capping agents made from S.alternifolium leaf extract may also be the cause of the aggregation behavior.

The nanoscale size and very uniform distribution of the particles were further confirmed by the SEM image at higher magnification. Because it can offer a greater active surface area and more reactive sites for interaction with dye molecules and microbial cells, the observed porous and aggregated shape is beneficial for photocatalytic and antibacterial applications. During photocatalytic reactions, the development of linked nanoparticle clusters may also improve charge transfer mechanisms.

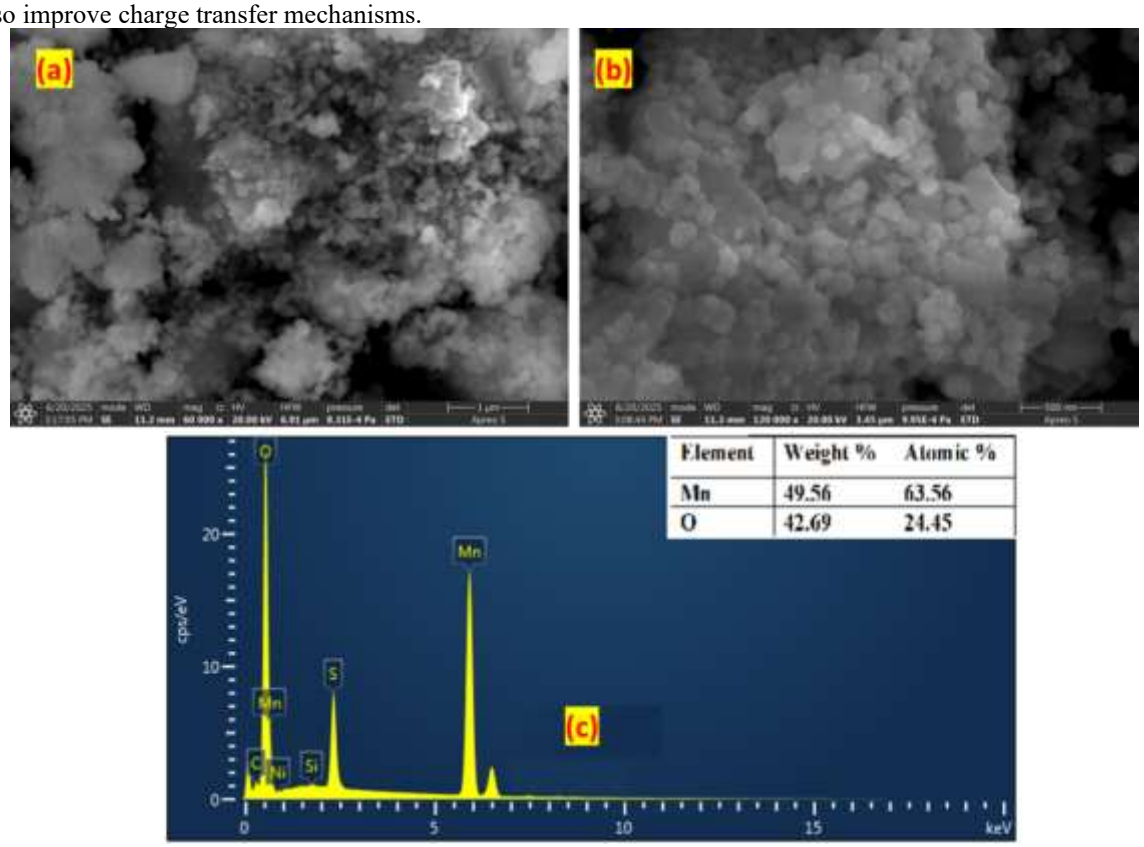

Fig.3: SEM (a,b), and EDX (c) images of Mn_2O_3 NPs

The synthesis of manganese oxide nanoparticles was confirmed by the EDX spectra, which showed that manganese (Mn) and oxygen (O) were the main constituent elements. Mn and O had weight percentages of 49.56% and 42.09%, respectively, according to the elemental composition analysis; the corresponding atomic percentages were 63.56% and 24.45% (Fig.3c). The effective production and purity of manganese oxide nanostructures were confirmed by the strong Mn and O signals. Additionally, minor peaks for sulfur (S), silicon (Si), nickel (Ni), and carbon (C) were seen; these could be the result of instrumental/sample holder contributions during SEM-EDX analysis, residual plant biomolecules, or precursor contaminants.

e. TGA study

The thermogravimetric analysis (TGA) curve of biosynthesized Mn_2O_3 NPs showed the thermal stability of material and breakdown behavior at a temperature range of up to 1000 ^oC, presented in Fig.4. The removal of physically adsorbed moisture and volatile chemicals from the surface of the nanoparticles is responsible for the initial weight loss seen below 150 ^oC. The breakdown of leftover organic macromolecules, including phenols, flavonoids, and other phytochemical components derived from the S.alternifolium leaf extract utilized during green synthesis, is represented by a slow weight loss between around 150 ^oC and 400 ^oC. The development of thermally stable manganese oxide nanoparticles with little additional breakdown is indicated by a comparatively steady plateau seen between 400 and 700 ^oC. The elimination of tightly bonded organic residues or small structural changes within the oxide lattice could be the cause of the tiny weight loss at higher temperatures [1].

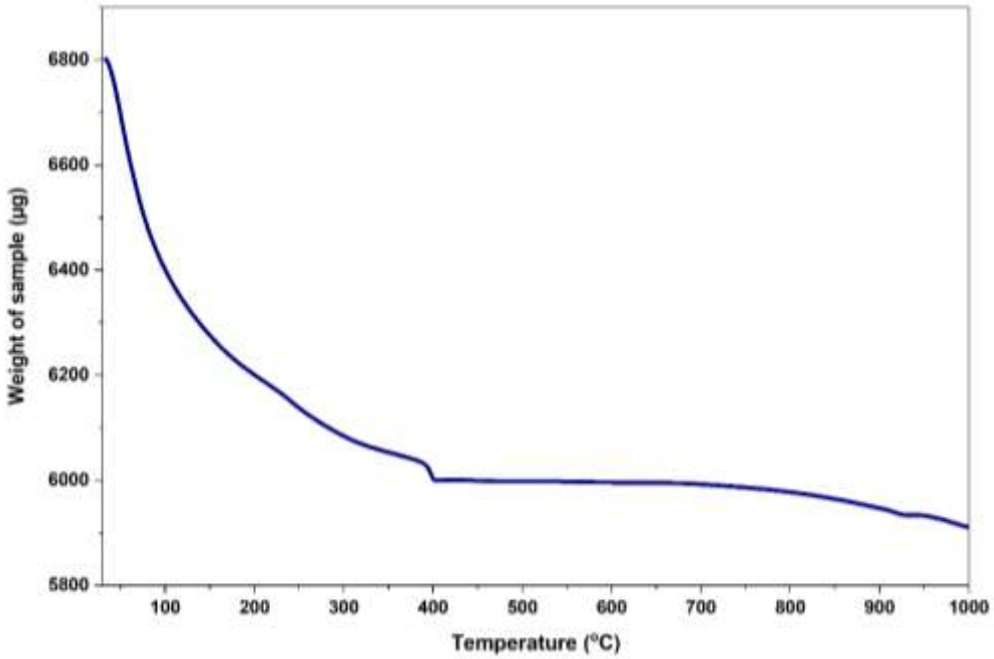

Fig.4: Thermogram curve of prepared Mn_2O_3 NPs

f. UV-Vis spectrum analysis

Figure 5 displays the UV-visible absorption spectrum of the biosynthesized Mn_2O_3 NPs. The spectra showed a strong UV absorption band with a noticeable peak at 229 nm, which is typical of manganese oxide NPs and verifies their successful production. The optical activity and light absorption capacity of the produced nanoparticles were also demonstrated by a broad absorption shoulder that extended toward the visible range. Charge transfer transitions between manganese and oxygen ions within the Mn_2O_3 crystal lattice may be responsible for the absorption characteristic. The particles' good dispersion and nanoscale properties are indicated by the absorbance gradually decreasing with increasing wavelength. The existence of tiny nanoparticles with potential surface flaws and phytochemical capping molecules derived from Syzygium alternifolium leaf extract is further suggested by the wide absorption profile [17]. The biosynthesized Mn_2O_3 NPs have advantageous optical characteristics for visible light-driven photocatalytic applications, as seen by the increased absorption in both the UV and visible areas.

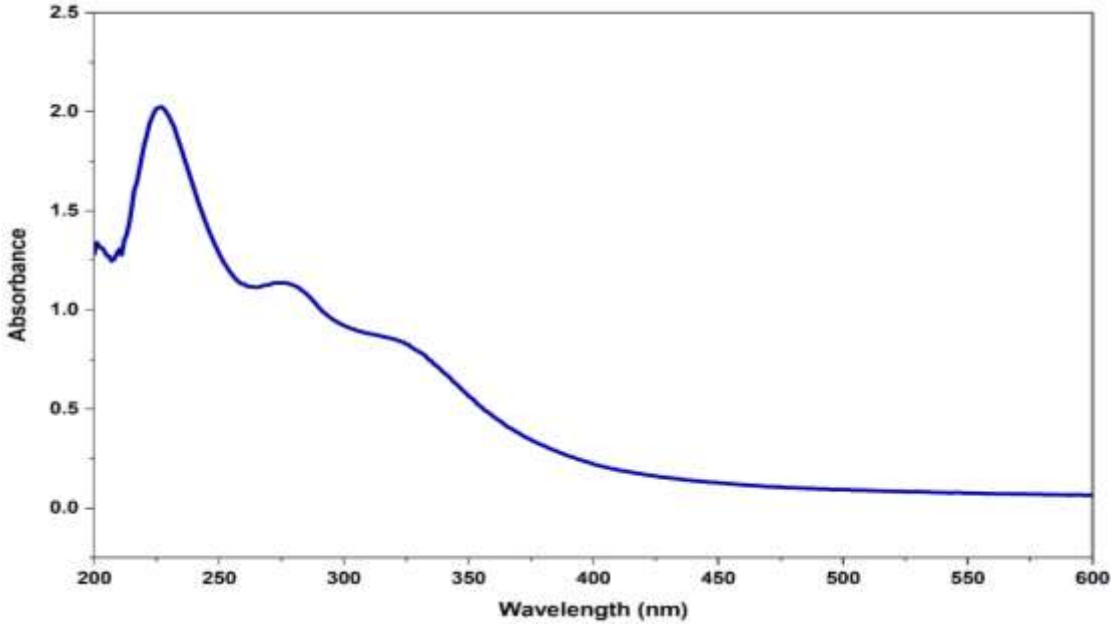

Fig.5: UV-Vis absorption spectrum of biosynthesized Mn_2O_3 NPs

6.2.2. Photocatalytic degradation of Crystal violet dye

The biosynthesized Mn_2O_3 NPs were further examined their photocatalytic performance towards the degradation of crystal violet (CV) dye under visible light irradiations, with conditions of 50 mg catalyst, 10 mg/L (ppm) of initial CV dye. The maximum absorbance of CV dye was observed at 590 nm. The degradation efficiency was monitored using UV-Vis absorption spectra with wavelength on x-axis and absorbance on y-axis. However, the

complete degradation needs to be studied the optimized conditions like pH, catalyst load, and dye initial concentration [1].

a. pH effect

Fig.6. demonstrated that the degradation efficiency increased progressively with irradiation time, signifying the effective photocatalytic performance of the synthesized Mn_2O_3 NPs. Nearly 98.9% of the CV dye was degraded in 80 minutes at pH-9, the highest degradation efficiency among the investigated pH values. In contrast, at pH-5, 7, and 11, degradation efficiencies of roughly 51.9%, 76.8%, and 85.6% were noted. The increased production of reactive oxygen species (ROS), especially hydroxyl radicals (•OH), which actively contribute to dye degradation, may be the cause of the improved photocatalytic efficiency in alkaline circumstances. Reduced hydroxyl ion availability and less contact between the catalyst surface and dye molecules may be the cause of the decreased degradation seen in acidic environments.

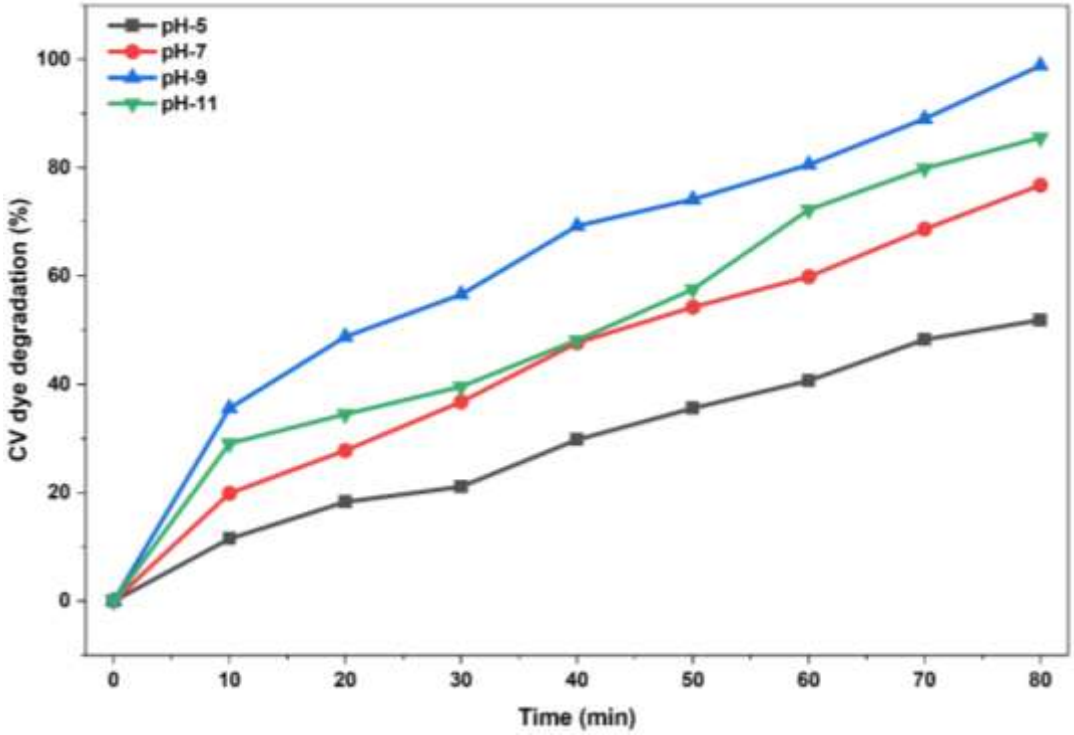

Fig.6: Effect of pH on degradation of CV dye

b. catalyst loading

Using biosynthesized Mn_2O_3 NPs, the impact of catalyst dosage on the photocatalytic degradation of CV dye under visible light irradiation is demonstrated in Fig.7. For all catalyst dosages, the degradation efficiency rose gradually with irradiation time, demonstrating the produced Mn_2O_3 NPs efficient photocatalytic activity. To find the ideal dosage for maximal dye degradation, several catalyst dosages of 30, 50, 70, and 100 mg were examined. Because more active surface sites were available and more ROS were produced, higher catalyst loading among the studied doses led to improved degrading efficiency [1]. Degradation efficiencies of roughly 80%, 99%, 100%, and 96% were attained at 80 minutes of irradiation for catalyst doses of 30, 50, 70, and 100 mg, respectively. At 70 mg, the most degradation was noted, indicating the ideal catalyst concentration for effective photocatalytic activity.

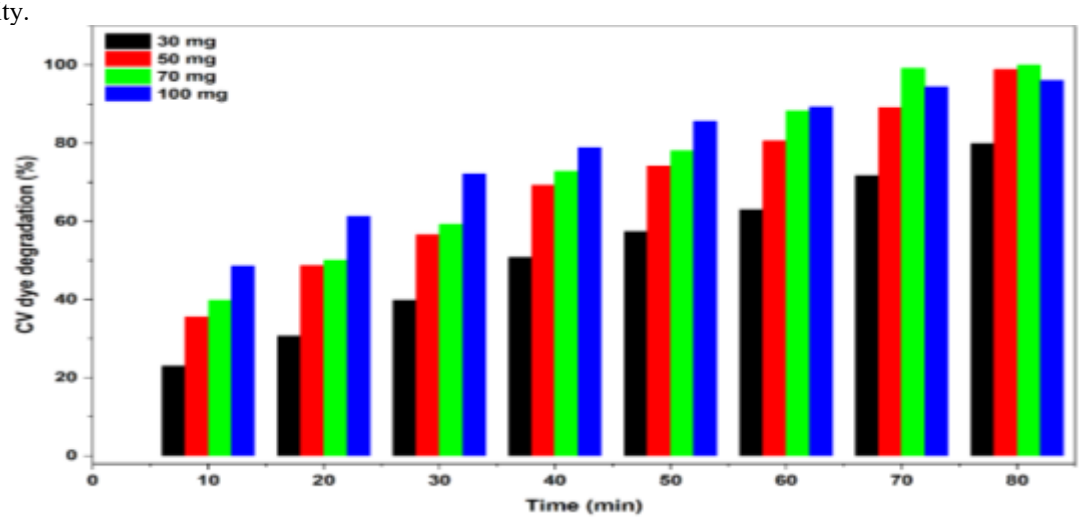

Fig.7: Effect of Mn_2O_3 NPs loading on degradation of CV dye

Up to 70 mg of catalyst, the degradation efficiency increased; however, at 100 mg, a small decrease was noted. This decline could be explained by high catalyst loading, which lowers photocatalytic performance by producing particle agglomeration, light scattering, and decreased visible light penetration into the reaction media.

c. CV dye initial concentration

Fig.8 illustrates how the initial concentration of CV dye affects the photocatalytic degradation efficiency of biosynthesized Mn_2O_3 NPs under visible light irradiation. For all measured dye concentrations, the degradation efficiency rose with irradiation time, demonstrating the produced nanoparticles' efficient photocatalytic activity. To assess their impact on the degradation process, initial dye concentrations of 5, 10, 20, and 30 mg/L were examined. The lowest dye concentration (5 mg/L) showed the highest degradation efficiency among the tested concentrations, reaching almost total disintegration (nearly 100%) after 70 minutes after irradiation. In contrast, after 80 minutes, degradation efficiencies of roughly 99%, 76%, and 66% were noted for dye concentrations of 10, 20, and 30 mg/L, respectively. The increasing number of dye molecules vying for active catalytic sites and the decreased visible light penetration through the reaction medium could be the cause of the decrease in degradation efficiency at higher dye concentrations [1, 6]. Dye molecules degrade more quickly at lower dye concentrations because there are more active sites on the catalyst surface available for the production of ROS. Nevertheless, the solution gets more strongly colored as the dye concentration rises, which restricts the photocatalyst's ability to absorb light and lowers photocatalytic effectiveness.

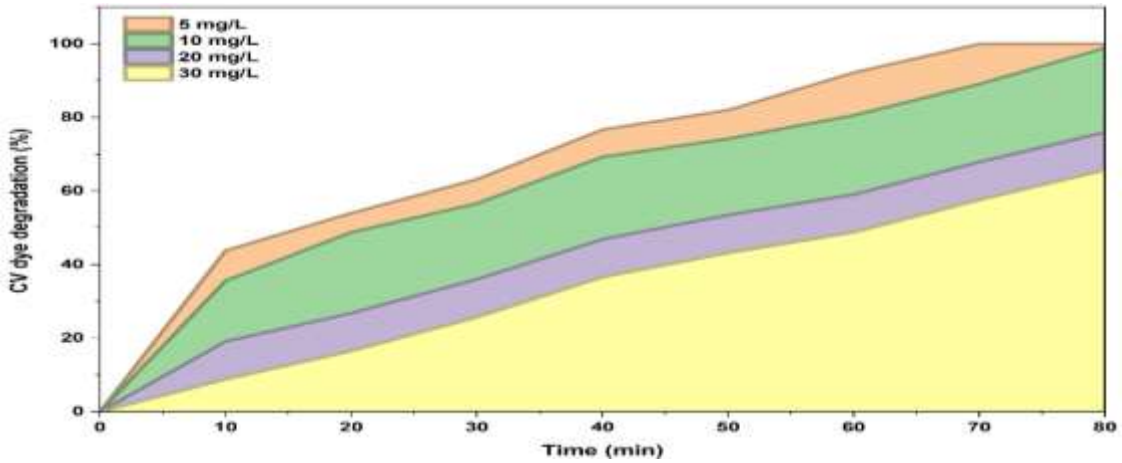

Fig.8: Effect of CV dye initial concentration using Mn_2O_3 NPs

d. Reusable study

The results are shown in Fig.9. Five sequential photocatalytic degradation cycles of crystal violet (CV) dye under visible light irradiation were used to assess the stability and reusability of the biosynthesized Mn_2O_3 NPs. The catalyst maintained significant photocatalytic activity even after repeated usage, however the degradation efficiency progressively declined as the number of reuse cycles increased. The Mn_2O_3 NPs reached a maximum degrading efficiency of 98.9% in 80 minutes during the first cycle; for the second, third, fourth, and fifth cycles, the corresponding efficiencies were 96%, 92.9%, 88.3%, and 82.4%.

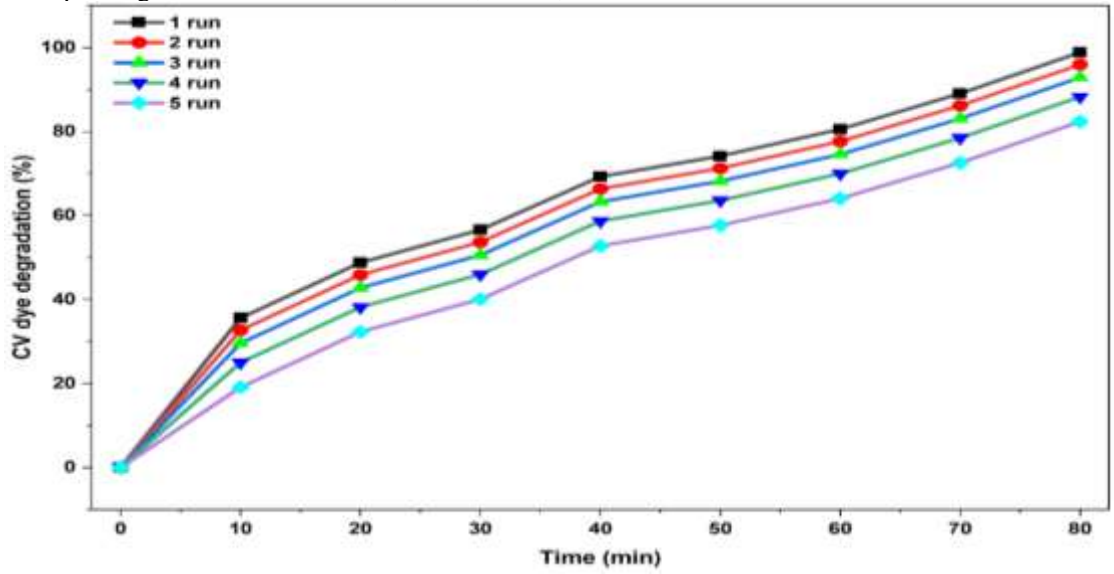

Fig.9: Reusability tests (5 cycles) over CV dye degradation

Agglomeration of nanoparticles, which can limit the number of active catalytic sites available for photocatalytic reactions, surface fouling by intermediate degradation products, and partial catalyst loss during recovery could all be responsible for the slight decrease in degradation efficiency following subsequent cycles. Even after the fifth

cycle, the Mn_2O_3 NPs retained over 80% degrading efficiency despite this slow fall, demonstrating exceptional structural stability and recyclability under visible light.

The findings demonstrate the biosynthesized Mn_2O_3 NPs great reusability and long-term photocatalytic stability, which makes them promising sustainable photocatalysts for real-world wastewater treatment applications. Their economic and environmental benefits for large-scale dye remediation methods are highlighted by their capacity to maintain high degradation efficiency after several cycles.

e. Stability assay

By comparing the XRD patterns of the fresh catalyst (first run) and the reused catalyst after the fifth cycle, as illustrated in Fig.10, the structural integrity of the biosynthesized Mn_2O_3 NPs following repeated photocatalytic use was examined. Even after several photocatalytic degradation cycles, the crystalline structure of Mn_2O_3 NPs was largely retained, as evidenced by the virtually similar position and strength of the diffraction peaks seen in both patterns. Without the emergence of notable impurity peaks or phase transformation, the distinctive peaks associated with the cubic α-Mn_2O_3 phase were evidently preserved. The overall diffraction pattern did not change after the fifth cycle, despite minor changes in peak intensity and broadening, demonstrating the superior structural stability and phase purity of the produced nanoparticles after repeated photocatalytic processes.

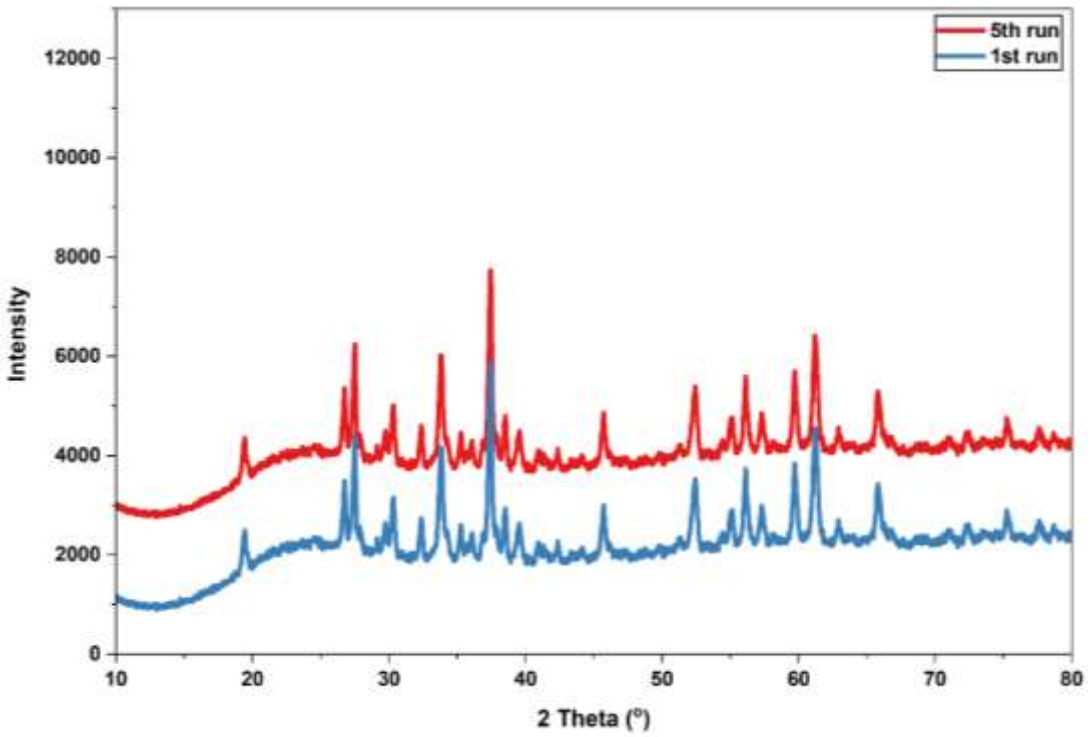

Fig.10: Stability test of biosynthesized Mn_2O_3 NPs

The high durability and recyclability of biosynthesized Mn_2O_3 NPs under visible light irradiation are demonstrated by the retention of crystalline properties after many cycles. These results validate Mn_2O_3 NPs as stable and effective photocatalysts for long-term wastewater treatment applications and corroborate the outstanding reusability performance seen in the photocatalytic degradation tests.

f. Probable mechanism

The photocatalytic degradation of CV dye over biosynthesized Mn_2O_3 NPs under visible light irradiation proceeds through semiconductor-mediated charge transfer process [1]. When visible light photons are absorbed by biosynthesized Mn_2O_3 NPs, electrons (e^-) in the valence band (VB) are excited to conduction band (CB). Leaving positive holes (h^+) in VB, thereby generates e-h pairs. The photoexcited e^- migrate to surface of Mn_2O_3 and are trapped by dissolved oxygen molecules (O_2) to form superoxide radical anions ($\bullet O_2^-$). These radicals further react with H_2O or H^+ to produce hydroxyl radicals ($\bullet HO_2$) and subsequently hydroxyl radicals (•OH). Meanwhile the photogenerated holes (h^+) oxidize surface-bound H_2O or OH^- ions to generate OH radiclas. The highly reactive $\bullet O_2^-$, $\bullet HO_2$, •OH radicals non-selectively attack the CV dye molecules, leading to the cleavage of chromophoric bound, N-CH_3 groups and aromatic rings, and ultimately mineralize the dye into CO_2, H_2O and other inorganic ions. The synergy between the ROS and the strong oxidizing holes ensures efficient degradation of CV dye. The small particle size. High surface area, and good visible-light absorption capacity of Mn_2O_3 NPs enhance charge separation, reduce electron-hole recombination, and provide abundant active sites for the generation of reactive species, resulting in excellent photocatalytic performance, as discussed in Fig.11.

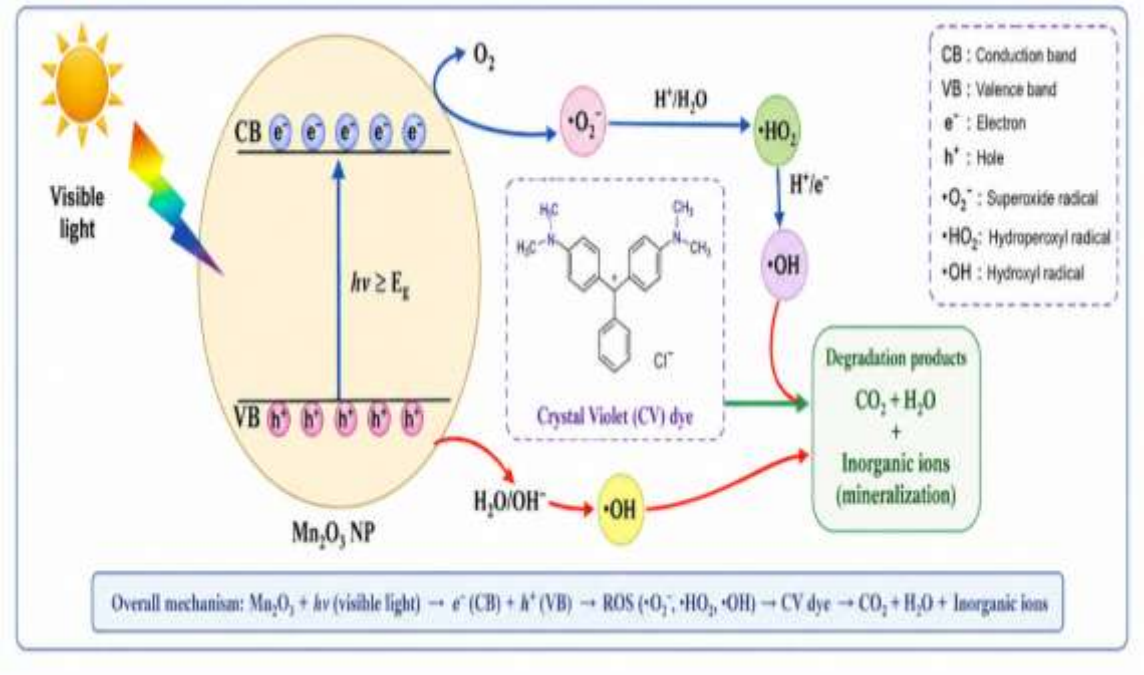

Fig.11: Photocatalytic degradation of CV dye using Mn_2O_3 NPs

The biosynthesized Mn_2O_3 NPs produced in this study showed very effective photocatalytic degradation of crystal violet (CV) dye under visible light irradiation, according to a comparison with previously published nanoparticle-based photocatalysts. At an initial dye concentration of 10 mg/L, the produced Mn_2O_3 NPs achieved over 99% degradation in 80 minutes, which is on par with or superior to a number of documented photocatalytic systems. While green-synthesized α-Mn_2O_3 NPs demonstrated nearly 96% degradation efficiency under visible light, previous research using Ag-decorated manganese oxide catalysts under sunlight irradiation indicated about 95% degradation. Similarly as presented in Table 1, TiO_2, Cu_2O, and $NiFe_2O_4$-based nanomaterials have also demonstrated significant photocatalytic activity toward CV degradation under different irradiation conditions.

Table 1: Comparative photocatalytic degradation of CV dye using various NPs

Photocatalyst	**Dye Concentration (mg/L)**	**Light Source**	**Degradation Efficiency (%)**	**Time (min)**	**Ref**
Syzygium- Mn_2O_3 NPs (present study)	10	Visible	99	80	Present work
Ag-decorated MnO_2 (Ag-OMS)	100	Sunlight	95	120	[18]
Green synthesized α-Mn_2O_3 NPs	10	Visible	~96	90	[19]
Cu_2O nanoparticles	20	Visible	66.58	60	[20]
TiO_2 nanoparticles	10	UV	~90	120	[21]
Honey-assisted $NiFe_2O_2$ NPs	10	Visible	~94	90	[22]

6.2.2. Antibacterial performance

Using the disc diffusion method, the antibacterial efficacy of Syzygium alternifolium-mediated Mn_2O_3 NPs was assessed against two clinically significant bacterial pathogens, Escherichia coli (Gram-negative) and Staphylococcus aureus (Gram-positive), at three different concentrations (10, 50, and 100 µg/mL). Standard antibiotic discs were used as a positive control (Fig.12). The biosynthesized Mn_2O_3 NPs showed quantifiable antibacterial activity against both test organisms in a concentration-dependent manner across all tested doses, according to the results, which are presented in Table 2.

Table 2: Antibacterial performance of Syzygium alternifolium-mediated Mn_2O_3 NPs

Sps.	**Zone of Inhibition (mm)**			
	Control	**10 µg/mL**	**50 µg/mL**	**100 µg/mL**
S.aureus	28	18	20	21
E.coli	28	20	21	22

The standard antibiotic's baseline bactericidal efficacy was demonstrated by the positive control, which showed zones of inhibition of 28 mm against both S.aureus and E.coli. The Mn_2O_3 NPs generated inhibition zones of 18 mm and 20 mm against S. aureus and E.coli, respectively, at the lowest measured dose of 10 µg/mL. The zones of inhibition showed a little but steady increase to 20 mm (S.aureus) and 21 mm (E.coli) upon raising the concentration to 50 µg/mL, suggesting a progressive improvement of antibacterial activity with increasing NP concentration. The inhibition zones grew to 21 mm against S.aureus and 22 mm against E.coli at the highest tested concentration of 100 µg/mL, demonstrating the dose-dependent link between nanoparticle concentration and antibacterial activity.

Fig.12: Antibacterial performance of prepared Mn_2O_3 NPs

Interestingly, at all examined concentrations, E.coli consistently showed marginally wider zones of inhibition than S.aureus. The two animals' fundamentally differing cell wall architectures may be the cause of this differential susceptibility. In contrast to the thick, multilayered cell wall of Gram-positive organisms, the relatively thinner peptidoglycan layer of Gram-negative bacteria may allow the nanoparticles to penetrate and interact with the bacterial membrane more quickly, increasing their bactericidal effect [23]. The production of reactive oxygen species (ROS), such as hydroxyl radicals (•OH) and superoxide anions ($O_2^{\bullet-}$), which cause oxidative stress, damage membrane integrity, obstruct enzymatic activity, and ultimately result in cell death, is the main mechanism by which Mn_2O_3 NPs work against bacteria. Furthermore, the intrinsic antimicrobial qualities of the phytochemical capping agents derived from S.alternifolium leaf extract primarily phenolics, flavonoids, and tannins may work in concert with the metal oxide core to enhance the overall bactericidal activity of the biosynthesized nanoparticles. The observed antibacterial activity is noteworthy and supports the potential of S.alternifolium-mediated Mn_2O_3 NPs as promising candidate nanomaterials for antimicrobial applications, especially in light of the global rise of antibiotic-resistant pathogens, even though the zones of inhibition produced by the Mn_2O_3 NPs at all concentrations were comparatively lower than those of the standard control.

Conclusions

In conclusion, Syzygium alternifolium leaf extract used as a natural reducing and stabilizing agent, the current study successfully demonstrated the green synthesis of Mn_2O_3 NPs. The successful synthesis of crystalline, thermally stable Mn_2O_3 NPs with nanoscale morphology and good elemental purity was validated by the systematic characterization of the produced nanoparticles using UV–Vis spectroscopy, XRD, FTIR, SEM–EDX, and TGA studies. The creation of cubic α-Mn_2O_3 NPs was indicated by XRD analysis, agglomerated spherical nanostructures were visible in SEM pictures, and the existence of manganese and oxygen as the primary elements was confirmed by EDX spectra.

Excellent visible-light-driven photocatalytic activity was demonstrated by the biosynthesized α-Mn_2O_3 NPs in the breakdown of crystal violet dye. Operational factors such pH, catalyst dosage, dye concentration, and irradiation period had a significant impact on the degradation efficiency. Under ideal circumstances, especially at alkaline pH, a maximum degradation efficiency of almost 99% was attained, indicating the potent catalytic potential of the produced nanoparticles. The production of reactive oxygen species, such as superoxide and hydroxyl radicals, which successfully mineralized the dye molecules, was primarily responsible for the photocatalytic degradation mechanism. The nanoparticles' outstanding stability and reusability were further confirmed by the fact that they maintained a sizable amount of photocatalytic activity even after five consecutive reuse cycles.

The produced Mn_2O_3 NPs shown significant antibacterial activity against both Gram-positive S.aureus and Gram-negative E.coli in addition to their photocatalytic capabilities. The antibacterial activities of the nanoparticles were concentration-dependent and could be linked to oxidative stress, membrane disruption, and the production of reactive oxygen species. Conclude that, the work shows that green-synthesized Mn_2O_3 NPs made from S.alternifolium are an environmentally benign, economical, and versatile nanomaterial with potential uses in antimicrobial therapy and wastewater treatment.

References

[1] S.M. Botsa, Adv. Compos. Hybrid Mater. 2025, 8(5), 384.
[2] M.M.H. Masum, M.B. Islam, M.R. Anowar, et al., Discov. Environ. 2025, 3, 59.
[3] M. Kumar, V.P. Singh, S.B. Bhat, et al., Discov. Environ. 2025, 3, 132.
[4] S. Al-Hadeethy, A.Z. Abdulmajeed, A.M. Alalusi, A.M. Mahdi, W.N. Hussain, I.A. Alrazaq, RSC Adv. 2025, 15, 48509–48520.
[5] S. Mani, R.N. Bharagava, in Reviews of Environmental Contamination and Toxicology, Vol. 237; W. de Voogt, Ed.; Springer: Cham, 2016, 71–104.
[6] A.B. Siddique, M.A. Shaheen, S. Shafeeq, A. Abbas, Y. Zaman, M.Z. Ishaque, M. Aslam, Mater. Adv. 2025, 6, 1330–1344.
[7] A.A. Miad, S.P. Saikat, M.K. Alam, M.S. Hossain, N.M. Bahadur, S. Ahmed, Nanoscale Adv. 2024, 6, 4781-4803.
[8] R.A. Kristanti, T. Hadibarata, A.G. Niculescu, D.E. Mihaiescu, A.M. Grumezescu, Nanomaterials 2025, 15(14), 1133.
[9] S.E.A. Elashery, I. Ibrahim, H. Gomaa, M.M. El-Bouraie, I.A. Moneam, S.S. Fekry, G.G. Mohamed, Magnetochemistry 2023, 9, 56.
[10] S. Muzammal, A. Ahmad, M. Sheraz, J. Kim, S. Ali, M.B. Hanif, I. Hussain, S. Pandiaraj, A. Alodhayb, M.S. Javed, H.A.Z. Al-bonsrulah, M. Motola, Energy Convers. Manage.: X 2024, 22, 100547.
[11] T. Naseem, T. Durrani, Environ. Chem. Ecotoxicol. 2021, 3, 59-75.
[12] T. Divya, S.S.Prashanna, S.Niveditha, K.Venkatachalam, Catal. Lett. 2025, 155, 347.
[13] S.N. Vavilapalli, S.S. Rani, G. Mamidi, S.M. Botsa, Next Nanotechnol. 2026, 9, 100463.
[14] S. Kumar, M. Kumar, V. Chauhan, D. Kaushal, Hybrid Adv. 2025, 10, 100475.
[15] G.I. Edo, A.N. Mafe, A.B.M. Ali, P.O. Akpoghelie, E. Yousif, E.F. Isoje, U.A. Igbuku, K. Zainulabdeen, J.O. Owheruo, A.E.A. Essaghah, H. Umar, D.S. Ahmed, A.A. Alamiery, Nano TransMed, 2025, 4, 100080.
[16] D. Shao, X. Li, M. Yang, J. Li, R. Chen, X. Zheng, Y. Niu, Y. Qi, Colloids Surf., A 2023, 658, 130532.
[17] I.A. Baba, O.B. Awe, S. Mustapha, M.A. Abubakar, A.S. Abdulkareem, J.O. Tijani, K.S. Obayomi, Hybrid Adv. 2026, 13, 100666.
[18] M. Saeed, R.D.C. Pecho, S. Panchal, S.K. Alhag, L.A. Al-Shuraym, K.M. Al Syaad, U.H. Bhutta, Water 2023, 15, 2480.
[19] S. Taghavi Fardood, F. Moradnia, F. Yekke Zare, S. Heidarzadeh, M.A. Majedi, A. Ramazani, M. Sillanpää, K. Nguyen, Sci. Rep. 2024, 14, 6755.
[20] P. Sharma, S. Kar, M. Sahu, M. Ganguly, RSC Adv. 2025.
[21] S.N. Ndung'u, E.W. Kinuthia, J. Water Environ. Technol. 2025.
[22] S.G. Divakara, B. Mahesh, H. Anil Kumar, Mater. Res. Express 2025.
[23] S.M. Botsa, K. Basavaiah, Sci. Rep. 2020, 10, 14080.